

Comparison of Decanethiolate Gold Nanoparticles Synthesized by One-Phase and Two-Phase Methods

Yuan Sun,[†] Anatoly I. Frenkel,[‡] Henry White,[†] Lihua Zhang,[§] Yimei Zhu,[§] Huiping Xu,[‡] Judith C. Yang,[‡] Tadanori Koga,[†] Vladimir Zaitsev,[†] Miriam H. Rafailovich,^{*,†} and Jonathan C. Sokolov[†]

Department of Materials Science and Engineering, State University of New York at Stony Brook, Stony Brook, New York 11794-2275, Department of Physics, Yeshiva University, New York, New York 10016, Center for Functional Nanomaterials, Brookhaven National Laboratory, Upton, New York 11973-5000, and Department of Materials Science and Engineering, University of Pittsburgh, Pittsburgh, Pennsylvania 15261

Received: January 20, 2006; In Final Form: July 26, 2006

We investigated the differences between the decanethiolate gold nanoparticles synthesized by two different routes: one-phase and two-phase methods. Their properties were compared in bulk and at the air–water interface by transmission electron microscopy (TEM), X-ray reflectivity (XR), extended X-ray absorption fine structure (EXAFS) spectroscopy, X-ray powder diffraction (XRD), thermal gravimetric analysis (TGA), time-of-flight secondary-ion mass spectrometry (TOF–SIMS), electron paramagnetic resonance (EPR), and Langmuir–Blodgett technique. The mean nanoparticles sizes obtained by EXAFS and XRD were found to be smaller than those by the TEM measurements. We explained these differences by the structural disorder and multiple twinning in the nanoparticles. The one-phase particles were found by EXAFS to be smaller and had a higher grafting density of thiol chains than the two-phase particles. We attributed these differences to the enhanced disorder of the one-phase particles. At the air–water interface, the one-phase particles did not spread, while the two-phase particles spread and formed Langmuir films. TEM and XR results revealed that the close-packed monolayer of the two-phase particles collapsed and folded into multilayer films upon further compression.

1. Introduction

Nanoscale particles have attracted remarkable research interest due to their unique properties and potential applications in catalysis, optical, magnetic, and electronic devices.^{1–6} In the past few years, a lot of semiconductor nanoparticles, such as silicon, germanium, and cadmium sulfide, and diverse metallic nanoparticles including copper, zinc, nickel, cobalt, iron, rhodium, palladium, platinum, gold, and silver were synthesized and studied. In particular, much attention has been paid to the synthesis of stable colloidal gold. Combining a two-phase approach introduced by Faraday⁷ with ion extraction and monolayer self-assembly of alkanethiol, Brust et al.⁸ developed a mild method for the synthesis of alkanethiol-functionalized gold nanoparticles, which is now widely used. However, this method is not suitable for ω -substituted thiols because of the difficulty in product purification. Yee et al.⁹ overcame this problem by exploring a novel one-phase method with no phase-transfer reagent involved in the system.

To understand the physical and chemical properties of alkanethiolate gold nanoparticles synthesized by the one-phase (Yee et al.⁹) and two-phase (Brust et al.⁸) routes, a systematic comparison between the results obtained by different synthetic techniques is needed. In this paper, we report our synthesis of the decanethiolate gold nanoparticles by both one-phase and

two-phase methods under the condition of the same initial Au/thiol mole ratio (1:2). As suggested before,^{8,9} these gold nanoparticles comprise gold cores with face-centered cubic (fcc) structure and monolayer self-assembly of thiol covering the cores. In principle, the surface of the nanoparticles should be highly hydrophobic because of the thiol coating. However, we were surprised to find that the particles made by the two-phase method were easily spread at the air–water interface producing uniform Langmuir films. To understand the differences between the two synthesis methods, we compared particles made by the two techniques using a battery of complementary methods: transmission electron microscopy (TEM), extended X-ray absorption fine structure (EXAFS), X-ray powder diffraction (XRD), and thermal gravimetric analysis (TGA) were used to compare the particle sizes, core structures, Au–Au and Au–S bonding properties, and the thiol coverage. X-ray reflectivity (XR) was used to characterize the Langmuir–Blodgett films produced from the two-phase particles at different surface pressures. Time-of-flight secondary-ion mass spectrometry (TOF–SIMS), the most sensitive surface analysis technique, was used to determine the quantitative elemental or isotopic composition of the nanoparticle surfaces.

Although the decanethiolate gold nanoparticles made by the one-phase and two-phase methods were protected by the same ligand and had similar sizes, they varied in grafting density and behavior at the air–water interface. The comparison helps us in selecting an appropriate synthesis method according to various purposes and specific properties of the nanoparticles.

* Corresponding author e-mail: miriam.rafailovich@sunysb.edu.

[†] State University of New York at Stony Brook.

[‡] Yeshiva University.

[§] Brookhaven National Laboratory.

[‡] University of Pittsburgh.

2. Experimental Section

2.A. Particle Synthesis. The decanethiolate gold nanoparticles were synthesized using two methods: (1) a one-phase method developed by Yee et al.⁹ and (2) a two-phase method developed by Brust et al.⁸ In the one-phase method, 2.0 mmol of decanethiol was added under vigorous stirring (about 1000 rpm) to a solution of 1.1 mmol of hydrogen tetrachloroaurate(III) trihydrate ($\text{H}[\text{Au}(\text{Cl}_4)] \cdot 3\text{H}_2\text{O}$) in 30 mL of freshly distilled, anhydrous THF. The mixture was stirred for about 20 min at room temperature. A volume of 20 mL of a 1.0 M solution of lithium triethylborohydride in THF was added at a rate of 0.1 mL/min. The mixture turned dark purple immediately. After being stirred for 3 h, the mixture was mixed with 200 mL of absolute ethanol to precipitate the nanoparticles. The particles were centrifuged and washed with ethanol four times and dried in a vacuum desiccator.

In the two-phase method, an aqueous solution of $\text{H}[\text{Au}(\text{Cl}_4)] \cdot 3\text{H}_2\text{O}$ (1.1 mmol in 36 mL of H_2O) was mixed with a solution of tetraoctylammonium bromide in toluene (4.8 mmol in 96 mL of toluene). The two-phase mixture was vigorously stirred until all the tetrachloroaurate was transferred into the organic layer. A volume of 2.0 mmol of decanethiol was then added. A freshly prepared aqueous solution of sodium borohydride (12 mmol in 30 mL of water) was added at a rate of 2 mL/min under vigorous stirring; the organic phase changed color from orange to deep brown within a few minutes. After being stirred for 3 h the organic phase was separated, evaporated to 5 mL in a rotary evaporator, and mixed with 200 mL of ethanol to remove excess thiol. The mixture was centrifuged to get the dark brown precipitate, which was washed with ethanol four times and dried in a vacuum desiccator.

Both the one- and two-phase decanethiolate gold nanoparticles were used as made with no further attempts to narrow the size distribution.

2.B. Measurement of the Surface Pressure/Area Isotherm. The surface pressure/area isotherm was measured at room temperature using a KSV 5000 LB trough with a pair of automatically movable barriers. The water was purified by a Millipore Milli-Q system. A volume of 250 μL of a 1 mg/mL solution of nanoparticles in toluene was spread uniformly onto the air–water interface. After the toluene evaporated, the isotherm measurement was initiated by double-barrier compression at a rate of 5 mm/min.

2.C. TEM Characterization. TEM analysis was performed on a Philips CM12 TEM operating at 100 keV. High-resolution TEM analysis was carried out on a JEOL 3000F operating at 300 keV, located at the Center for Functional Nanomaterials, Brookhaven National Laboratory, and a JEOL 2010F operating at 200 keV, located at the Materials Research Laboratory, University of Illinois at Urbana-Champaign. The samples were prepared in two different ways. A droplet of dilute solution of nanoparticles in toluene was evaporated onto the carbon-coated side of a 400 mesh copper TEM grid. For Langmuir films of nanoparticles, the edge of a grid was clamped with tweezers and brought parallel to the surface of the trough. The carbon-coated side was quickly contacted with the film surface and lifted off.

2.D. Time-of-Flight Secondary-Ion Mass Spectrometry (TOF–SIMS). The samples were prepared as thin films of nanoparticles drop-cast on a $5 \times 5 \text{ mm}^2$ silicon wafer treated by aqueous hydrofluoric acid. Time-of-flight secondary-ion mass spectroscopy measurements were performed on a CAMECA TOF–SIMS IV equipped with a ^{69}Ga gun. The primary ion energy and the average current were 15 keV and 0.25 pA,

respectively. The pulsed primary ion beam (27 ns pulse, 100 μs cycle) was rastered (256×256 raster) over the area of $500 \times 500 \mu\text{m}^2$ at the center and edge of the dried film of nanoparticles on the silicon wafer. Negative secondary-ion mass spectra in the mass range of 1–600 Da were measured and combined from 25 scans.

2.E. X-ray Reflectivity (XR). To study the Langmuir films of the two-phase gold nanoparticles formed under specific surface pressures, films were lifted from the water surface onto silicon wafers and measured by X-ray reflectivity.

The scattering geometry of the wave vector components used in the experiments were explained in our previous paper.¹⁰ The specular reflectivity is sensitive to the dispersion profile, δ , perpendicular to the interfaces; thus, the details of the out-of-plane structure of the gold nanoparticles in the Langmuir films can be revealed.

The samples for the XR measurements were prepared as follows. At the desired surface pressure, the Langmuir–Blodgett (LB) technique was used to transfer the Langmuir film of the two-phase gold nanoparticles from the air–water interface onto a 2 in. \times 2 in. silicon wafer (treated by a sulfuric acid–hydrogen peroxide mixture), which was immersed in the pure water before the particle solution was spread and then retracted at a speed of 2 mm/min. The measurements were performed on beamline X10B of the National Synchrotron Light Source at Brookhaven National Laboratory, using a 0.2 mm \times 0.5 mm X-ray beam of wavelength $\lambda = 0.87 \text{ \AA}$.

2.F. X-ray Powder Diffraction. X-ray powder diffraction (XRD) data were taken with $\text{Cu K}\alpha$ radiation ($\lambda = 1.5418 \text{ \AA}$) on a SCINTAG/PAD-V diffractometer in the $30\text{--}90^\circ$ (2θ) range with a step size of $\Delta 2\theta = 0.05^\circ$ and scan rate of $1^\circ/\text{min}$. Samples were prepared as uniform thin films supported on microscope slides from drop-casting of toluene solutions dried in air. The sizes of the Au nanoparticles were estimated by X-ray diffraction peak line width broadening using the Scherrer formula for very small crystals.¹¹ All X-ray data were fit to Gaussian line shapes with PeakFit (SYSTAT Software Inc.).

2.G. Extended X-ray Absorption Fine Structure (EXAFS). All X-ray absorption data were collected using beamline X16C at the National Synchrotron Light Source, Brookhaven National Laboratory. The sample was prepared by uniformly spreading ca. 10 mg of the particles over a ca. 20 cm long adhesive tape with a brush. The tape was folded several times to reach an appropriate thickness for transmission EXAFS experiments, corresponding to the Au L_3 absorption edge step of ca. 0.5. X-ray absorption data from the sample and a reference thin gold foil were measured in transmission mode at room temperature by scanning from 150 eV below to 1200 eV above the Au L_3 -edge (11 917 eV). The reference Au foil was used to calibrate the beam energy during each scan of the Au L_3 -edge. The analysis of EXAFS data was performed by IFEFFIT.¹²

2.H. Thermal Gravimetric Analysis (TGA). NETZSCH STA449C was used. The heating rate was $2^\circ\text{C}/\text{min}$ from room temperature to 100°C , then $10^\circ\text{C}/\text{min}$ to 800°C .

2.I. Electron Paramagnetic Resonance (EPR). The EPR spectra were recorded on a Bruker ESP380E spectrometer, equipped with an HP 5361 frequency counter operating at X-band, at room temperature, using the following parameters: microwave power, 0.67 to $\sim 0.7 \text{ mW}$; modulation amplitude, 33 G; scan times, 8; modulation frequency, 100 kHz; time constant, 1.28 ms; sweep time, up to 168 s; sweep width, 7000 G; X-axis resolution, 4 K. The particles were measured in EPR tubes. The starting material $\text{H}[\text{Au}(\text{Cl}_4)] \cdot 3\text{H}_2\text{O}$ and blank EPR tube were run as control samples.

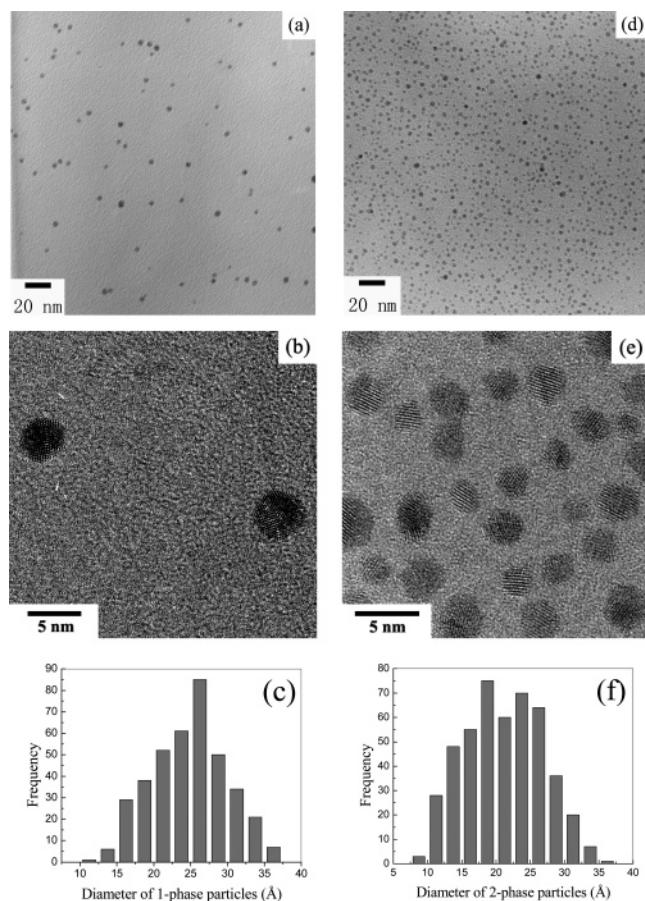


Figure 1. TEM images, HRTEM images, and core size distribution histograms of (a–c) one-phase particles and (d–f) two-phase particles. The average core sizes are 25 ± 5 Å and 21 ± 6 Å for the one-phase and two-phase particles, respectively.

3. Results and Discussion

3.A. TEM, HRTEM, and Electron Diffraction. TEM and HRTEM images of the one- and two-phase particles dried from dilute toluene solutions and the core size distribution histograms are given in Figure 1. The one-phase particles have a mean size of 25 ± 5 Å (excluding the thiol coating). The two-phase particles have a smaller mean size of 21 ± 6 Å. We fixed the initial ratio of H[Au(CI₄)] to decanethiol as 1:2 for both methods to make sure there are enough thiols in the reaction system to be used as ligands to cover the gold cores. Therefore, under the condition of the same Au/thiol ratio, the one-phase method results in particles with larger mean size, although the size distribution is medium for both methods. As shown in Figure 1, parts b and e, and Figure 2, the HRTEM images and electron diffraction patterns reveal the highly crystalline structure (fcc) for both particles, with the cell parameter a_0 of 4.07 Å, which is very close to that of bulk gold (4.0786 Å from X-ray diffraction¹³). We also noticed that about 50% of the one-phase particles had twinned or multitwinned structures inside the gold cores, while twins existed in about 30% of the two-phase particles. Figure 3a shows the HRTEM lattice image of a relatively large one-phase particle consisting of four twin domains labeled by A, B, C, and D, and four twin boundaries indicated by the straight lines. The twinning relationship between twin domains A and B can be clearly seen since their twin plane (111) is edge on. Figure 3b shows the twinning and twin domains in a two-phase particle. The corresponding diffractogram is shown in Figure 3c, where the reflections of twin

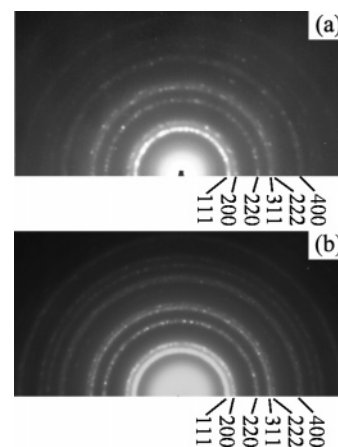


Figure 2. Electron diffraction patterns of (a) one-phase and (b) two-phase particles. The patterns can be indexed to an fcc structure with a cell parameter a_0 of 4.07 Å.

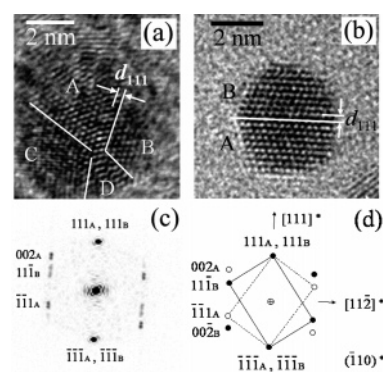


Figure 3. HRTEM lattice image of (a) a one-phase particle consisting of more than two twin domains and (b) a two-phase particle with (111) twinning, where the straight lines are the twin boundaries; (c) the corresponding diffractogram of image (b) where reflections of twin domains A and B are indicated; (d) analysis of the twinning relationship of the particle in (b), where (*) refers to the reciprocal space.

domains A and B are indicated, respectively. The analysis of the twinning relationship is shown in Figure 3d. The stacking of close-packed atomic planes adjacent to the invariant plane of (111), as marked as a straight line in Figure 3b, reflects their mirror symmetry. The twin A is rotated respect to the twin B 180° about the [112] axis. The facets of this particle are clearly visible. The (002) and (111) planes in both twin domains A and B suggest low surface energies in these lattices. One can also notice that some of the reflection spots in Figure 3c are elongated due to the sudden change of the lattice orientation across the twin boundary.

In thermal gravimetric analysis (TGA), the thiol coating will be totally burnt away since we increase the temperature to 800 °C; only pure gold will be left. Therefore, thiol coverage could be determined, although it relies on how accurately the core size can be measured. Considering the TEM-measured mean size as the average core size and the density of 0.059 Au atoms per Å³ as bulk gold, the number of thiol chains per particle is determined to be about 237 and 70, based on a TGA weight loss of 30.98% and 17.77% for the one- and two-phase particles, respectively. Therefore, the average molecular weight of the particles is approximate 132 870 and 68 464 g/mol for the one- and two-phase particles, respectively.

3.B. Surfaces of the Nanoparticles. According to the surface pressure versus area (π -A) isotherms shown in Figure 4, the

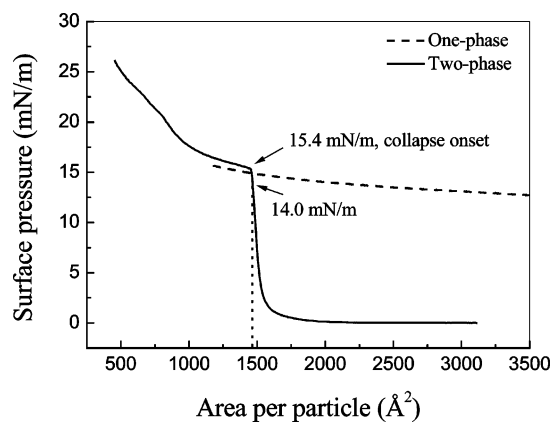


Figure 4. Isotherm π - A diagrams of the decanethiolate Au nanoparticles.

TABLE 1: Negative Secondary-Ion Intensities of Bromine and Gold (Normalized to Gold Intensity)

	two-phase nanoparticles		one-phase nanoparticles	
	edge	center	edge	center
^{79}Br	14.273×10^{-3}	6.634×10^{-4}	2.506×10^{-4}	2.259×10^{-4}
^{81}Br	13.555×10^{-3}	5.897×10^{-4}	2.327×10^{-4}	2.050×10^{-4}
Au	1	1	1	1

two-phase decanethiolate particles behave differently as compared with one-phase particles. Acting like amphiphilic molecules, the two-phase particles spread at the air–water interface and produce a π - A curve very similar to the one we previously obtained from the dodecanethiolate palladium nanoparticles made from the two-phase method.¹⁰ However, the one-phase particles do not spread on the water, which is consistent with their hydrophobic surfaces rising from the thiol coating. One possible explanation for this difference may be the relatively lower thiol graft density of two-phase particles and dramatically high thiol grafting density of one-phase particles, as we obtain from the EXAFS and TGA results and discuss in section 3.E. Therefore, the surfaces of the two-phase particles are less hydrophobic and could wet the air–water interface. Another possibility may be very small remnants of some hydrophilic headgroups on the surfaces of two-phase particles which further assists the particles to spread at the air–water interface. They could be a small amount of the phase-transfer reagent, tetraoctylammonium bromide (TOABr), which is only used in the two-phase method. During the synthesis procedures, a very small amount of TOABr may be absorbed onto the surface of gold nanoparticles through the interdigitation of the octyl chains with the alkyl chains of thiol^{14,15} and the strong adsorption of Br^- ion on gold.¹⁶ The amount of TOABr is less than 1%¹⁴ and hence could not be detected using proton NMR¹⁷ or in our case EXAFS. We therefore used TOF-SIMS, where the cross section for Br is much higher than for the other elements in our samples and concentrations on the order of parts per million could be detected. The one-phase particles were used as the control sample since there was not any source of bromine introduced in the one-phase method. The negative secondary-ion intensities of bromine and gold measured from the edge and the center of the dried particle films were given in Table 1. We can see that the intensities of ^{79}Br and ^{81}Br of the two-phase particles were about 3–5 times larger than those of one-phase particles with nearly the same intensities of Au. Therefore, we could speculate that the existence of trace of TOABr on the surface of two-phase nanoparticles might assist the particles to spread at the

air–water interface. Waters et al.¹⁴ and Leff et al.¹⁷ also found the existence of TOABr in their nanoparticles made from the two-phase method.

One may think that this trace amount of TOABr is a “contaminant” resulting from the two-phase synthesis procedure. Some methods used for particle size separation are expected to provide further purification, such as size-selective precipitation and column chromatography, as summarized by Murray et al.¹⁸ Recently, Waters et al.¹⁴ found that Soxhlet extraction with acetone was an effective purification method. Will these methods thoroughly remove the small amount of TOABr from the nanoparticles? Heath et al. treated their two-phase Au and Ag nanoparticles by the size-selective precipitation,¹⁹ however, their nanoparticles still formed Langmuir films at the air–water interface. Even after a 12 h extraction, approximately 5×10^{-3} % of TOABr remained in Waters et al.’s sample.¹⁴ Therefore, a very small amount of TOABr could be tenaciously retained by the nanoparticles, even if advanced purification was conducted.

3.C. Langmuir Monolayer of the Two-Phase Particles.

Langmuir monolayers prepared at the air–water interface from other nanoparticles such as gold,^{19–24} silver,^{19,25a} cadmium sulfide,^{25b} and cadmium selenide²⁶ have been reported. It is interesting to point out that the two-phase method was widely used to make the gold nanoparticles.^{19,21,22} Even though well-ordered Langmuir films were reported, few studies were performed to investigate the structures of the films.²⁷ To understand the Langmuir films produced from our two-phase gold particles in greater detail, we studied the structures and thickness of these films and distribution of the ligands around the gold cores using TEM and X-ray reflectivity.

The π - A isotherm for this system is shown in Figure 4. From the figure we can see that the system has a relatively sharp plateau at 15.4 mN/m and is nearly flat at lower pressures, indicating that there is nearly no gas phase before a transition to a solid, incompressible state is achieved. Further decrease of the area per particle A to 1438 Å is seen to collapse the film with a slow increase in pressure, indicating that hard core interactions are now present. To understand the structure of the particles responsible for these transitions, we lifted films from the air–water interface onto carbon-coated TEM grids at surface pressures of 2.0, 14.0, and 19.0 mN/m and examined them using TEM. The images are shown in Figure 5, from where we can calculate directly the area per particle, A , at different pressures, π . We find that $A = 2700$ Å for $\pi = 2$ mN/m and $A = 2400$ Å for $\pi = 14.0$ mN/m. At higher pressures, the particles seem to have aggregated into cylindrical structures, and it is difficult to determine the area of individual particles. We can therefore conclude that the area per particle does not change appreciably below the plateau. In the image obtained from film lifted at the lowest pressure, we see large holes or voids in the film. We therefore believe that the nanoparticles self-assemble into islands almost immediately after spreading. These islands are even visible as purplish domains at the air–water interface. The particles within the islands are already interdigitated with the interparticle spacing mostly depending on the thiol chain length. As the surface area is decreased, the islands are brought together and the water between them is eliminated. Hence no real “gas” phase of disordered particles exists, which would produce an area-dependent surface pressure. Once the islands have merged, the film becomes rigid and a sharp increase in surface pressure is observed. Further decreasing the surface area causes the film to buckle, and small cylindrical agglomerates of particles are observed in Figure 5c.

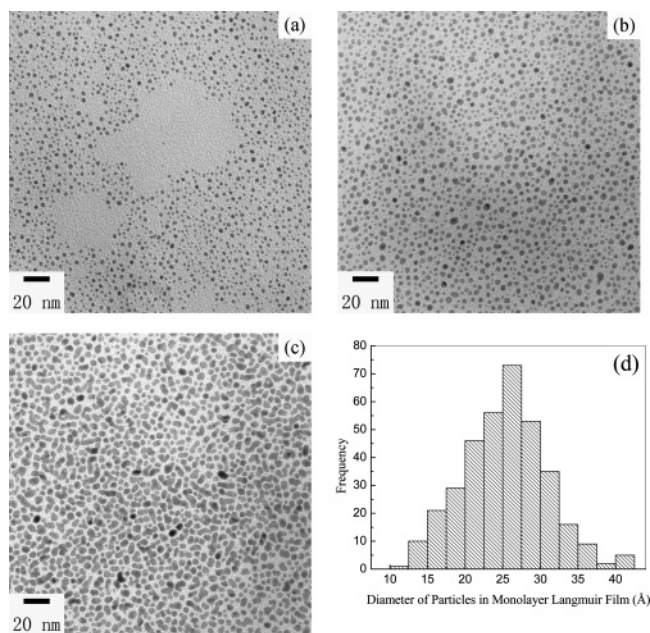


Figure 5. TEM images of the two-phase particles in Langmuir films formed under (a) 2.0 mN/m, (b) 14.0 mN/m, (c) 19.0 mN/m, and (d) core size distribution histogram of particles in Langmuir monolayer (formed under 14.0 mN/m).

The Langmuir films of the two-phase nanoparticles formed under surface pressure of 14.0, 16.0, and 25.0 mN/m were also deposited onto silicon wafers, and their structure was measured using X-ray reflectivity. The data are shown in Figure 6a, where measured reflectivity is plotted as a function of twice the glancing angle of incidence (2θ). The data for $\pi = 14.0$ mN/m were fit using a 6-layer model consisting of Si, SiO₂, thiol (hydrocarbon), Au/thiol, thiol, and air, respectively, while data for $\pi = 16.0$ and 25.0 mN/m were fit using 8- and 10-layer models, respectively. The fitting functions are plotted in Figure 6e–g, while the fitting parameters are given in Table 2. From the data we see that good agreement with a monolayer fit is obtained for the film obtained at a surface pressure of 14.0 mN/m. The thickness of the Au/thiol layer is about 13.6 Å, which can be considered as the diameter of the nanoparticles in the direction (Z) normal to the surface. However, as given in Figure 5b, the TEM micrograph of nanoparticles in the monolayer Langmuir film shows a slightly larger average diameter of 25.3 Å, or similar to the value, 21 Å, obtained for the particles prior to spreading. This suggests that the particles become oblate after spreading at the air–water interface with an axial ratio of 0.54 (Figure 6b). A similar phenomenon was observed on the dodecanethiolate palladium nanoparticles we previously made from the two-phase method.¹⁰

From Figure 6b we see that the best fit is obtained when the Au/thiol layer is sandwiched between two thiol layers, whose thicknesses are 8.1 and 6.2 Å at the SiO₂ and air interfaces, respectively. Both of them are less than 13.2 Å, or the length of a fully extended decanethiol chain,²⁸ which suggests the thiol chains are not perpendicular to the surface of the nanoparticle. The electron density, δ , of the thiol layers is nearly the same as that of the bulk thiols. Hence there are no voids in either of the layers. We can then calculate the grafting density on each particle. The volume of the shell is approximately 22 314.6 Å³ due to the oblate ellipsoid model of the nanoparticle in Figure 6b. The length of the fully extended decanethiol chain is about 13.2 Å,²⁸ and the surface area footprint of a thiol ligand is 21.4 Å²,²⁹ thus, the volume of one fully extended decanethiol chain

is 282.48 Å³. Consequently, there are 79 thiol chains in the shell coating each particle. This number is in good agreement with the TGA result of 70 thiol chains per particle.

The dispersion value of the Au/thiol layer, $\delta_{\text{Au/thiol}}$, is best fit to be 4.33×10^{-6} as shown in Figure 6e. Therefore, the gold cores occupy approximately a quarter volume of the mixed Au/thiol layer. In this LB monolayer, the average surface area occupied by one particle can then be estimated as 1330 Å², compared with 1468 Å² from the π - A diagram.

The measured reflectivity curve for the sample lifted at 16.0 mN/m, or into the plateau region, is shown in Figure 6a. From the figure we can clearly see that the oscillation frequency has nearly doubled indicating that the layer thickness has increased by nearly the same amount. As the film area is decreased, the structure of the Langmuir film changes from a simple monolayer to a bilayer. It is reasonable to assume that when the nanoparticles are squeezed, some of them will slide over the first monolayer to form a second layer on top. We then modify the 6-layer model by adding another two layers, Au/thiol and thiol, as shown in Figure 6c. The best fitting of the reflectivity gives $\delta_{\text{Au/thiol}}$ values of 4.33×10^{-6} and 1.07×10^{-6} for the bottom and top Au/thiol layers, respectively. This difference in $\delta_{\text{Au/thiol}}$ values indicates that the top nanoparticle layer is not fully covered by the gold nanoparticles as the bottom monolayer. We also notice that the $\delta_{\text{Au/thiol}}$ value and the thickness of the bottom Au/thiol layer are the same as that of the Au/thiol layer in the monolayer LB film.

For the film taken at 25.0 mN/m, the oscillations in the measured reflectivity curve have an even higher frequency and are somewhat irregular (Figure 6a), which hints the formation of a thicker, though disordered, Langmuir film, as the layer collapses. To fit the profile, we assumed a film structure with three layers of gold nanoparticles. These layers are further subdivided, and we see that the film is now comprised of 10 layers as shown in Figure 6d. The fitting parameters are given in Table 2.

3.D. X-ray Powder Diffraction. Figure 7 shows the XRD patterns for the one- and two-phase nanoparticles. The peaks at around 38°, 65°, and 78° are indexed as the (111), (220), and (311) reflections of the fcc structure, respectively. The (200) reflection is seen as a shoulder and can be separated from the (111) reflection by PeakFit. Then we use the full width at half-maximum (fwhm) of the (111) peak to estimate particle sizes by the Scherrer formula, neglecting the effect of the instrumental factor. The sizes of one- and two-phase particles are determined to be about 21.0 ± 0.4 Å and 17.1 ± 0.1 Å, respectively, which are very close to but slightly smaller than the TEM mean sizes (Table 3). This means there must be other minor factors which broaden the peak line width along with the size effect. These factors may include amorphous (disordered) structures and strain effect¹¹ inside the particles. Amorphous structures have been found in previous high-resolution electron microscopy studies on Au and Pd nanoparticles.^{30,31} Besides, the stability of disordered structures in isolated gold nanoclusters has been predicted by Garzón et al.,³² while the strain might be induced by the large surface tension of the particles.³³

The Au–Au interatomic distance $R(\text{Au–Au})$ is also calculated from the position of the (111) peak, then compared with the data we got from EXAFS in Table 4. According to the XRD and EXAFS measurements (discussed in section 3.E.), $R(\text{Au–Au})$ of both one- and two-phase nanoparticles are slightly shorter than that of bulk gold. This result can be explained by the relatively large surface tension of the nanoparticles that causes relaxation of the surface layer toward the core.³⁴

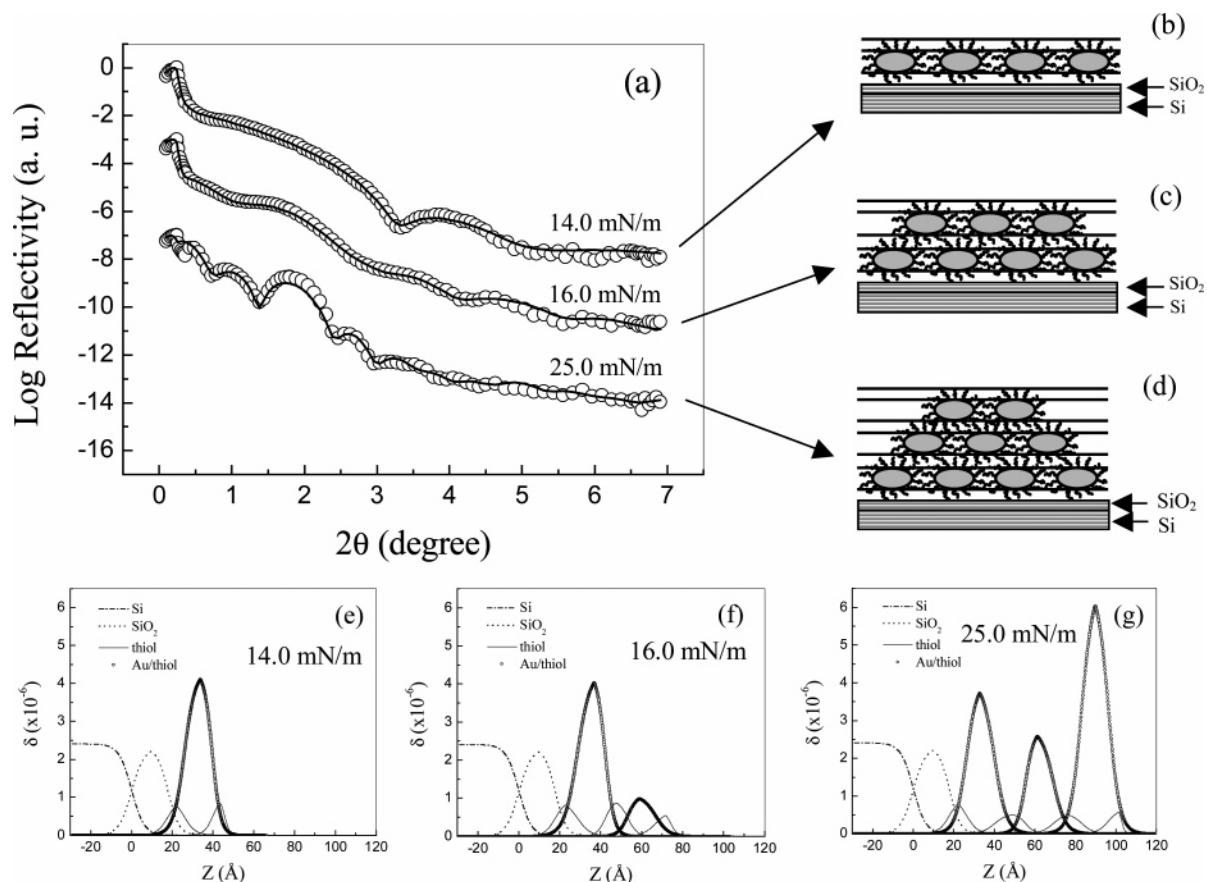


Figure 6. (a) Plot of the measured (empty circles) and the calculated (solid lines) reflectivities of the Langmuir films taken at surface pressures of 14.0, 16.0, and 25.0 mN/m. Schemes of the (b) 6-layer model, (c) 8-layer model, and (d) 10-layer model on silicon wafers. Dispersion profiles of each layer in the Langmuir films taken at (e) 14.0 mN/m, (f) 16.0 mN/m, and (g) 25.0 mN/m.

TABLE 2: X-ray Reflectivity Fitting Parameters of the Langmuir Films Formed From the Two-Phase Gold Nanoparticles Under Surface Pressures of 14.0, 16.0, and 25.0 mN/m, Where s Is the Roughness Upon Each Layer in Å, t Is the Average Thickness of a Layer in Å, and δ Is the Dispersion Component

	14.0 mN/m			16.0 mN/m			25.0 mN/m		
	s	t	$\delta \times 10^6$	s	t	$\delta \times 10^6$	s	t	$\delta \times 10^6$
Si substrate			2.239			2.239			2.239
SiO ₂	4.85	17.94	2.31	4.78	17.94	2.31	4.78	17.94	2.31
thiol	4.89	8.11	0.95	5.76	10.74	0.95	4.83	8.39	0.95
Au/thiol	3.66	13.66	4.33	3.80	13.68	4.33	5.39	13.86	4.05
thiol	2.12	6.15	0.95	4.16	10.96	0.95	3.88	15.38	0.52
Au/thiol				5.72	13.61	1.07	5.36	13.67	2.76
thiol				2.95	7.33	0.67	5.02	13.97	0.53
Au/thiol							4.92	13.26	6.58
thiol							1.46	6.43	0.65

3.E. EXAFS Analysis. The Fourier transforms (FTs) of all EXAFS data are presented in Figure 8. Characteristic signatures of the fcc structure in the reference Au foil data can be found in the FT spectra of both one- and two-phase nanoparticles. Data analysis was performed in R -space, within the distance range between 1.30 and 3.33 Å (uncorrected for the photoelectron phase shifts), which corresponds to the first nearest neighbor Au–S and Au–Au bonds only. Theoretical scattering amplitudes and phases of the photoelectron were calculated with the program FEFF6.³⁵ Data and best fits are shown in Figure 9. Results of the fitting are summarized in Table 5. The average coordination numbers of nearest Au–Au neighbors (CN(Au–Au)) of the one- and two-phase particles are 5.1 and 7.4, respectively, both smaller than 12, the number of first nearest neighbors in the bulk fcc Au lattice. This decrease is due to a high fraction of the surface gold atoms surrounded by less than

12 neighbors. Since the average coordination number of nearest neighbors (CN) in nanoparticles is a nonlinear function of the particle size,^{36–40} assuming a cuboctahedral structural motif of Au nanoparticles,⁸ these coordination numbers correspond to the particle sizes of 8.6 and 14.3 Å for the one- and two-phase particles, respectively.

As summarized in Table 3, the sizes measured from EXAFS are smaller than those from both XRD and TEM. Similar studies of polydispersed nickel^{41a} and platinum^{41b} nanoparticles by Calvin and co-workers also revealed that the mean size determined from EXAFS was smaller than those from XRD and TEM. As we proposed in section 3.D. that the disordered structures are responsible for the underestimation of the mean size by XRD, we believe that these amorphous structures also cause relatively lower coordination numbers than those of perfectly crystalline particles with the same sizes. Besides, due

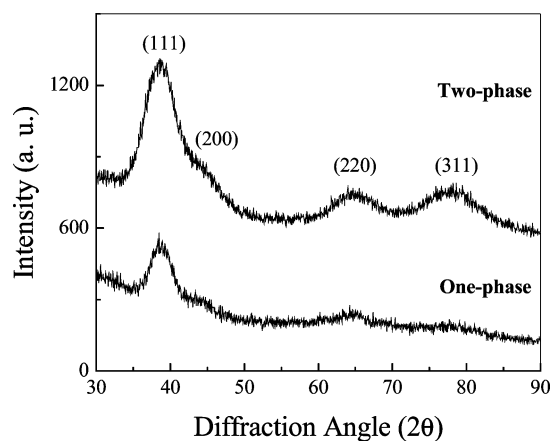


Figure 7. X-ray powder diffraction patterns for the one- and two-phase Au nanoparticles. The sizes are about 21.0 Å (one-phase particles) and 17.1 Å (two-phase particles).

TABLE 3: Comparison of the Sizes of the One- and Two-Phase Au Nanoparticles (Å), Measured by Different Instruments

	TEM	XRD	EXAFS
one-phase	25 ± 5	21.0 ± 0.4	8.6
two-phase	21 ± 6	17.1 ± 0.1	14.3

TABLE 4: Comparison of the Au–Au Interatomic Distance $R(\text{Au–Au})$ (Å) Measured by Different Instruments^a

	XRD	EXAFS
one-phase	2.84(1)	2.848(7)
two-phase	2.85(1)	2.824(8)
bulk Au	2.8840 ^b	2.860(2)

^a Uncertainties in the last digits are given in parentheses. ^b JCPDS-International Centre for Diffraction Data.

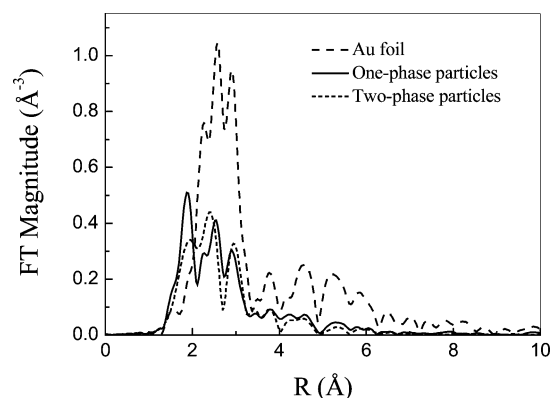


Figure 8. Fourier-transformed EXAFS data of the reference gold foil and the decanethiolate gold nanoparticles.

to multiple twins, we expect significant structural disorder in Au–Au bond lengths that are near the twin boundaries. Therefore, we underestimate the coordination numbers and thus determine smaller sizes for the particles with imperfections. We obtain that the one-phase particles have a higher fraction of disordered or defective structure according to the dramatic difference between the TEM and EXAFS mean size.

We have measured average particle sizes by three techniques: TEM, XRD, and EXAFS. Among them, the XRD and EXAFS methods have limitations in size determinations, while TEM as a direct tool would be more accurate. For the XRD method, crystallite sizes well determinable by line-broadening

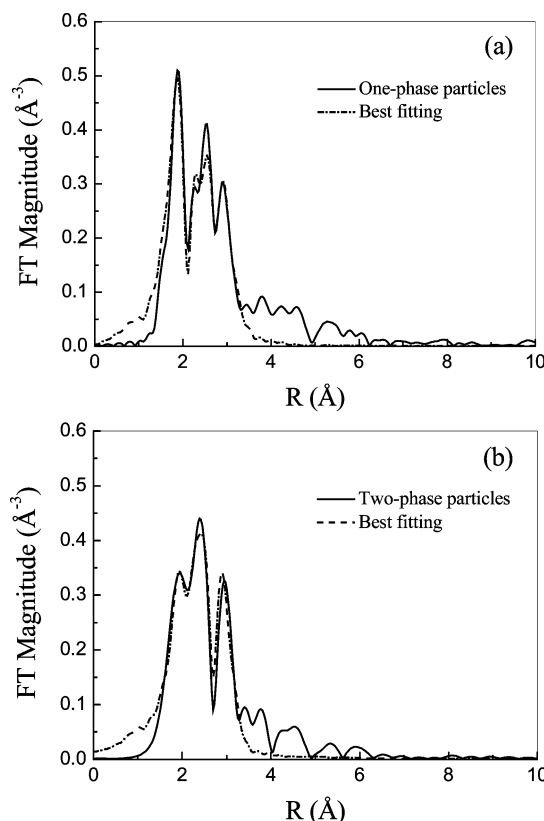


Figure 9. Data and FEFF6 fit of (a) one-phase and (b) two-phase particles.

analysis are in the range of 20–1500 Å. Besides, the determined size is a characteristic average from the crystallite size distribution. The Scherrer method used in this paper yields the volume-weighted size. For the EXAFS method, analysis of particle size is not conclusive for sizes larger than 40 Å. It will not distinguish such a particle from the bulk. In addition, EXAFS analysis will be hindered by the polydispersity of the particle sizes. The narrower the size distribution the more reliable are EXAFS results for the mean particle size. Therefore, EXAFS analysis should be done in combination with other structural techniques, e.g., TEM and XRD.

The distance of neighboring Au atoms $R(\text{Au–Au})$ was determined to be 2.848(7) and 2.824(8) Å for the one- and two-phase particles, respectively; both are significantly shorter than the value of 2.860(2) Å of bulk gold. As discussed previously, this shortening is caused by the lattice contraction of the nanoparticles due to surface tension, and it is consistent with what we observed in the XRD analysis. The one-phase particles have a smaller lattice contraction compared to that of the two-phase ones. Therefore, according to Mays et al.,⁴² the one-phase particles are expected to be larger in size, on the average, compared to the two-phase ones, which agrees with TEM and XRD measurements. Systematic investigation of the particle size effect on the first nearest neighbor distance shortening has been published elsewhere.⁴³

The presence of Au–S bonds (corresponding to the low- R peak in Figure 8) is also evident in the EXAFS data. Therefore, we included an extra contribution accounting for the Au–S shell in the fitting model. Their best-fit lengths and mean-square disorders are given in Table 5. Another parameter $\text{CN}(\text{Au–S})$, defined as the number of Au–S bonds divided by total number of Au atoms in a particle, can tell us the thiol coverage, provided that the total number of Au atoms per particle is known. The total number of Au atoms in one particle is estimated to be 466

TABLE 5: Summary of Results of EXAFS Refinements of Gold Foil and the Decanethiolate Gold Nanoparticles^a

	CN(Au–Au)	R(Au–Au) (Å)	σ^2 (Au–Au) (Å ²)	CN(Au–S)	R(Au–S) (Å)	σ^2 (Au–S) (Å ²)
gold foil	12	2.860(2)	0.0082(2)			
one-phase	5.1(8)	2.848(7)	0.010(1)	0.91(17)	2.283(8)	0.003(1)
two-phase	7.4(1.0)	2.824(8)	0.012(1)	0.43(16)	2.317(15)	0.003(3)

^a CN, *R*, and σ^2 are the coordination number, interatomic distance, and the standard deviation in the distance between the central (absorbing) Au atom and its nearest (S or Au) neighbors. Uncertainties in the last digits are given in parentheses.

and 286 for the one- and two-phase particles, respectively. This estimate was obtained from the TEM mean size assuming the density of 0.059 Au atoms per Å³ as bulk gold. Therefore, the number of Au–S bonds per particle is about 427 ± 79 and 123 ± 46 for the one- and two-phase particles, respectively. Assuming 3-fold binding sites of S, as on the Au (111) surface,⁴⁴ the number of thiol chains coating each particle can be conservatively estimated to be 140 ± 30 and 40 ± 15 for one- and two-phase particles, respectively. Compare this estimation with that obtained by TGA (section 3.A.): 237 and 70 for the one- and two-phase particles, respectively. We conclude that the actual structure of the binding sites is neither 3-fold nor on top, but between these two extremes.

Assuming the TEM-measured size is the average core size and the thiol chains cap the surface of the gold core evenly, we can also calculate the surface area occupied by one thiol chain. The value of the one-phase particles (8.1 Å^2) is extremely smaller than that of the two-phase particles (19.8 Å^2) and the flat Au(111) facet (21.4 Å^2).²⁹ It is known that the nanoparticles have a higher grafting density of thiol chains than a flat Au surface,^{45,46} due to the curved surfaces where a greater concentration of defect sites and higher radius of curvature help to bind more thiol chains. The grafting density of our two-phase particles is slightly higher but approaches that of a flat Au(111) surface. Similar observations have been made by Hostetler et al.^{47a} We believe that a larger proportion of edge and corner atoms⁴⁷ and a greater concentration of defect sites on the surfaces of the one-phase particles are responsible for the extremely high grafting density of these particles. The comparison of the TEM and EXAFS mean sizes already indicates that the one-phase particles have more defective structures than the two-phase particles.

As we mentioned in section 3.B., the one- and two-phase particles behave differently at the air–water interface, probably due to their different thiol grafting densities. The surfaces of the one-phase particles are hydrophobic because of the dramatically high thiol coverage, while the two-phase particles have lower and perhaps partial thiol coverage and therefore could wet the water surface and then spread to form Langmuir films.

3.F. Magnetism. Hori et al. have observed superparamagnetic behavior in 30 Å Au nanoparticles embedded in poly(*N*-vinyl-2-pyrrolidone) at low temperatures.⁴⁸ Lately, the direct evidence of the intrinsic ferromagnetism in 19 Å Au nanoparticles was found.⁴⁹ We therefore tried to measure the magnetic moment in our particles. We found that for both one- and two-phase particles, the amplitude of the EPR signals is very weak and similar to that of the Au salt and the blank tube, from which we believe that both particles do not have unpaired spins or a magnetic moment.

4. Conclusions

In this paper, we investigate the differences between the decanethiolate gold nanoparticles synthesized by one- and two-phase methods. Although both types of particles are covered

by the same type of ligand, their dimensions, thiol grafting density, and ability to form a film at the air–water interface are very different. TEM images indicate that the one-phase particles are approximately 25 Å in diameter, while the two-phase particles are 21 Å. EXAFS and TGA data reveal that each S atom bonds with more than one Au atom; in particular, the one-phase particles have a larger fraction of amorphous or defective structures and higher grafting density of thiol chains than the two-phase particles. XRD and EXAFS data indicate that the Au–Au interatomic distances of both one- and two-phase particles are slightly shorter than that of bulk gold. We attribute this behavior to the surface tension of the particles and the relaxation of the surface layer toward the core. EPR measurement indicates that no magnetic moments were observed in either case. One-phase particles dewet the air–water interface and do not form a uniform film. Two-phase particles spread easily at the air–water interface, and a surface pressure diagram can be generated. X-ray reflectivities of films lifted off the water surface using a Langmuir–Blodgett trough indicate that the particles form a uniform layer at low surface pressures, where the particles appear oblate in shape. Increasing the surface pressure produces an incompressible particle bilayer film, followed by a collapsed state.

Acknowledgment. This work was supported by the NSF-MRSEC program. A.I.F. acknowledges support by the U.S. DOE Grant No. DE-FG02-03ER15477. J.C.Y. and H.X. acknowledge support by the U.S. DOE Grant No. DE-FG02-03ER15475. Research was carried out in part at the Center for Functional Nanomaterials, Brookhaven National Laboratory, which is supported by the U.S. Department of Energy, Division of Materials Sciences and Division of Chemical Sciences, under Contract No. DE-AC02-98CH10886. The authors gratefully acknowledge the assistance of Dr. Chirakkal V. Krishnan, Xianzhong Guo, Hongwen Zhou, Dr. Lijun Wu, Avital Merl, and Dana Glasner. Access to the EPR equipment was provided by Dr. Ning Chi and Dr. Nan-Loh Yang in College of Staten Island of the City University of New York.

References and Notes

- (1) Schmid, G.; Ed. *Clusters and Colloids: From Theory to Applications*; VCH: Weinheim, Germany, 1994.
- (2) Fendler, J. H. *Membrane-Mimetic Approach to Advanced Materials*; Springer-Verlag: Berlin, 1994.
- (3) Dorogi, M.; Gomez, J.; Osifchin, R. G.; Andres, R. P.; Reifengerger, R. G. *Phys. Rev. B* **1995**, *52*, 9071.
- (4) Turton, R. *The Quantum Dot: A Journey into the Future of Microelectronics*; Oxford University Press: New York, 1995.
- (5) Jena, P.; Khanna, S. N.; Rao, B. K.; Eds. *Proceedings of the Science and Technology of Atomically Engineered Materials*; World Scientific: Singapore, 1996.
- (6) Dubertret, B.; Skourides, P.; Norris, D. J.; Noireaux, V.; Brivanlou, A. H.; Libchaber, A. *Science* **2002**, *298*, 1759.
- (7) Faraday, M. *Philos. Trans. R. Soc. London* **1857**, *147*, 145.
- (8) Brust, M.; Walker, M.; Bethell, D.; Schiffrin, D. J.; Whyman, R. *J. Chem. Soc., Chem. Commun.* **1994**, 801–802.
- (9) Yee, C. K.; Jordan, R.; Ulman, A.; White, H.; King, A.; Rafailovich, M.; Sokolov, J. *Langmuir* **1999**, *15*, 3486.

- (10) Sun, Y.; Frenkel, A. I.; Isseroff, R.; Shonbrun, C.; Forman, M.; Shin, K.; Koga, T.; White, H.; Zhang, L.; Zhu, Y.; Rafailovich, M. H.; Sokolov, J. C. *Langmuir* **2006**, *22*, 807–816.
- (11) Guinier, A. *X-ray Diffraction*; W. H. Freeman: San Francisco, CA, 1963.
- (12) Newville, M. J. *Synchrotron Radiat.* **2001**, *8*, 322.
- (13) JCPDS-International Centre for Diffraction Data.
- (14) Waters, C. A.; Mills, A. J.; Johnson, K. A.; Schiffrin, D. J. *Chem. Commun.* **2003**, *4*, 540–541.
- (15) Badia, A.; Cuccia, L.; Demers, L.; Morin, F.; Lennox, R. B. *J. Am. Chem. Soc.* **1997**, *119*, 2682–2692.
- (16) Pajkossy, T.; Wandlowski, T.; Kolb, D. J. *Electroanal. Chem.* **1996**, *414*, 209–220.
- (17) Leff, D. V.; Brandt, L.; Heath, J. R. *Langmuir* **1996**, *12*, 4723–4730.
- (18) Murray, C. B.; Kagan, C. R.; Bawendi, M. G. *Annu. Rev. Mater. Sci.* **2000**, *30*, 546–610.
- (19) Heath, J. R.; Knobler, C. M.; Leff, D. V. *J. Phys. Chem. B* **1997**, *101*, 189–197.
- (20) (a) Chi, L. F.; Rakers, S.; Hartig, M.; Fuchs, H.; Schmid, G. *Thin Solid Films* **1998**, *327*, 520–523. (b) Burghard, M.; Philipp, G.; Roth, S.; von Klitzing, K.; Pugin, R.; Schmid, G. *Adv. Mater.* **1998**, *10*, 842–845. (c) Vassiliev, A.; Rehage, H.; Schmid, G.; Neumeier, S.; Meyer-Zaika, W. *J. Cluster Sci.* **2005**, *16*, 379–390.
- (21) Bourgoin, J.-P.; Kergueris, C.; Lefèvre, E.; Palacin, S. *Thin Solid Films* **1998**, *327*, 515–519.
- (22) (a) Chen, S. *Adv. Mater.* **2000**, *12*, 186–189. (b) Chen, S. *Langmuir* **2001**, *17*, 2878–2884.
- (23) Fukuto, M.; Heilmann, R. K.; Pershan, P. S.; Badia, A.; Lennox, R. B. *J. Chem. Phys.* **2004**, *120*, 3446–3459.
- (24) (a) Huang, S.; Tsutsui, G.; Sakaue, H.; Shingubara, S.; Takahagi, T. *J. Vac. Sci. Technol., B* **2001**, *19*, 115–120. (b) Huang, S.; Minami, K.; Sakaue, H.; Shingubara, S.; Takayuki, T. *Langmuir* **2004**, *20*, 2274–2276.
- (25) (a) Meldrum, F. C.; Kotov, N. A.; Fendler, J. H. *Langmuir* **1994**, *10*, 2035–2040. (b) Kotov, N. A.; Meldrum, F. C.; Wu, C.; Fendler, J. H. *J. Phys. Chem.* **1994**, *98*, 2735–2738.
- (26) Gattás-Asfura, K. M.; Constantine, C. A.; Lynn, M. J.; Thimann, D. A.; Ji, X.; Leblanc, R. M. *J. Am. Chem. Soc.* **2005**, *127*, 14640–14646.
- (27) Nørgaard, K.; Weygand, M. J.; Kjaer, K.; Brust, M.; Bjørnholm, T. *Faraday Discuss.* **2004**, *125*, 221.
- (28) Whetten, R. L.; Shafiqullin, M. N.; Khoury, J. T.; Schaaff, T. G.; Vezmar, I.; Alvarez, M. M.; Wilkinson, A. *Acc. Chem. Res.* **1999**, *32*, 397.
- (29) Sellers, H.; Ulman, A.; Schnidman, Y.; Eilers, J. E. *J. Am. Chem. Soc.* **1993**, *115*, 9389–9401.
- (30) Tehuacanero, S.; Herrera, R.; Avalos, M.; Yacaman, M. J. *Acta Metall. Mater.* **1992**, *40*, 1663.
- (31) Krakow, W.; Yacamán, M. J.; Aragón, J. L. *Phys. Rev. B* **1994**, *49*, 10591.
- (32) Garzón, I. L.; Michaelian, K.; Beltrán, M. R.; Posada-Amarillas, A.; Ordejón, P.; Artacho, E.; Sánchez-Portal, D.; Soler, J. M. *Phys. Rev. Lett.* **1998**, *81*, 1600.
- (33) (a) Vermaak, J. S.; Mays, C. W.; Kuhlmann-Wilsdorf, D. *Surf. Sci.* **1968**, *12*, 128. (b) Woltersdorf, J.; Nepijko, A. S.; Pippel, E. *Surf. Sci.* **1981**, *106*, 64.
- (34) Edelstein, A. S.; Cammarata, R. C.; Eds. *Nanomaterials: Synthesis, Properties and Applications*; Institute of Physics Publishing: Bristol and Philadelphia, 1998.
- (35) Zabinsky, S. I.; Rehr, J. J.; Ankudinov, A.; Albers, R. C.; Eller, M. J. *Phys. Rev. B* **1995**, *52*, 2995–3009.
- (36) Clausena, B. S.; Topsøe, H.; Hansen, L. B.; Stoltze, P.; Nørskov, J. K. *Catal. Today* **1994**, *21*, 49–55.
- (37) Benfield, R. E. *J. Chem. Soc., Faraday Trans.* **1992**, *88*, 1107–1110.
- (38) Gregor, R. B.; Lytle, F. W. *J. Catal.* **1980**, *63*, 476–486.
- (39) Jentys, A. *Phys. Chem. Chem. Phys.* **1999**, *1*, 4059–4063.
- (40) (a) Frenkel, A. I. *J. Synchrotron Radiat.* **1999**, *6*, 293–295. (b) Frenkel, A. I.; Hills, C. W.; Nuzzo, R. G. *J. Phys. Chem. B* **2001**, *105*, 12689–12703.
- (41) (a) Calvin, S.; Miller, M. M.; Goswami, R.; Cheng, S.-F.; Mulvaney, S. P.; Whitman, L. J.; Harris, V. G. *J. Appl. Phys.* **2003**, *94*, 778–783. (b) Calvin, S.; Luo, S. X.; Caragianis-Broadbridge, C.; McGuinness, J. K.; Anderson, E.; Lehman, A.; Wee, K. H.; Morrison, S. A. *Appl. Phys. Lett.* **2005**, *87*, 233102.
- (42) Mays, C. W.; Vermaak, J. S.; Kuhlmann-Wilsdorf, D. *Surf. Sci.* **1968**, *12*, 134–140.
- (43) Frenkel, A. I.; Nemzer, S.; Pister, I.; Soussan, L.; Harris, T.; Sun, Y.; Rafailovich, M. H. *J. Chem. Phys.* **2005**, *123*, 184701.
- (44) Bain, C. D.; Biebuyck, H. A.; Whitesides, G. M. *Langmuir* **1989**, *5*, 723–727.
- (45) Dubois, L. H.; Nuzzo, R. G. *Annu. Rev. Phys. Chem.* **1992**, *43*, 437–463.
- (46) Badia, A.; Singh, S.; Demers, L.; Cuccia, L.; Brown, G. R.; Lennox, R. B. *Chem. Eur. J.* **1996**, *2*, 359–363.
- (47) (a) Hostetler, M. J.; Wingate, J. E.; Zhong, C.-J.; Harris, J. E.; Vachet, R. W.; Clark, M. R.; Londono, J. D.; Green, S. J.; Stokes, J. J.; Wignall, G. D.; Glish, G. L.; Porter, M. D.; Evans, N. D.; Murray, R. W. *Langmuir* **1998**, *14*, 17–30. (b) Terrill, R. H.; Postlethwaite, T. A.; Chen, C.-H.; Poon, C.-D.; Terzis, A.; Chen, A.; Hutchison, J. E.; Clark, M. R.; Wignall, G.; Londono, J. D.; Superfine, R.; Falvo, M.; Johnson, C. S., Jr.; Samulski, E. T.; Murray, R. W. *J. Am. Chem. Soc.* **1995**, *117*, 12537–12548.
- (48) Hori, H.; Teranishi, T.; Nakae, Y.; Seino, Y.; Miyake, M.; Yamada, S. *Phys. Lett. A* **1999**, *263*, 406–410.
- (49) Yamamoto, Y.; Miura, T.; Suzuki, M.; Kawamura, N.; Miyagawa, H.; Nakamura, T.; Kobayashi, K.; Teranishi, T.; Hori, H. *Phys. Rev. Lett.* **2004**, *93*, 116801.